

# EXPLORING LOW-RANK STRUCTURE FOR AN INVERSE SCATTERING PROBLEM WITH FAR-FIELD DATA\*

YUYUAN ZHOU<sup>†</sup>, LORENZO AUDIBERT<sup>‡</sup>, SHIXU MENG<sup>§</sup>, AND BO ZHANG<sup>†</sup>

**Abstract.** The inverse scattering problem exhibits an inherent low-rank structure due to its ill-posed nature; however developing low-rank structures for the inverse scattering problem remains challenging. In this work, we introduce a novel low-rank structure tailored for solving the inverse scattering problem. The particular low-rank structure is given by the generalized prolate spheroidal wave functions, computed stably and accurately via a Sturm-Liouville problem. We first process the far-field data to obtain a post-processed data set within a disk domain. Subsequently, the post-processed data are projected onto a low-rank space given by the low-rank structure. The unknown is approximately solved in this low-rank space, by dropping higher-order terms. The low-rank structure leads to a Hölder-logarithmic type stability estimate for arbitrary unknown functions, and a Lipschitz stability estimate for unknowns belonging to a finite dimensional low-rank space. Various numerical experiments are conducted to validate its performance, encompassing assessments of resolution capability, robustness against randomly added noise and modeling errors, and demonstration of increasing stability.

**Key words.** inverse scattering, low-rank, Helmholtz equation, generalized prolate spheroidal wave functions, Fourier integral, regularization

**1. Introduction.** Inverse scattering merits important applications in non destructive testing, seismic imaging, ocean acoustics, non destructive testing and many other areas. For a more comprehensive introduction, we refer to [10, 12]. This problem is very challenging due to its intrinsically ill-posed and nonlinear nature. In this work, we aim to mitigate this challenge by exploring the low-rank structure of the data. In a broader perspective, this is in the spirit of learning low dimensional feature spaces by deep learning [15] and kernel machine learning [13, 21]. We point out recent machine learning approaches to inverse scattering [14, 26, 30, 32, 33, 35].

Low-rank methods are capable of mitigating the curse of dimensionality for high dimensional PDEs, see for instance the monograph [20] and the survey [4]. For the inverse scattering problem and for inverse problems in general, exploring low-rank structures is a natural choice since the solution intrinsically has a low-rank structure due to its ill-posedness: putting it another way, one can think about solving a linear system with an ill-conditioned matrix and looking for a solution in a low dimensional space spanned by principal components. However unlike a simple linear system, it is much more difficult to study the low-rank structure for inverse scattering problems. The linear sampling method [11] and factorization method [27] are shape identification methods that recognize the nonlinear nature. Recently it was shown in [28] that the eigenvalues of the data operator and these of its linearized version (i.e., Born data operator) decay in the same rate. The work [34] also shares a similar spirit on the connection between the ill-posedness of the fully nonlinear model and the Born model. Thus important insights may be drawn from the Born model. The recent work [26] explored the low-rank structure of the (discretized) inverse scattering by a neural

---

\*Submitted to the editors May, 2024; updated December, 2024

<sup>†</sup>Academy of Mathematics and Systems Science, Chinese Academy of Sciences, Beijing, 100190, China and School of Mathematical Sciences, University of Chinese Academy of Sciences, Beijing 100049, China (zhouyuyuan@amss.ac.cn, b.zhang@amt.ac.cn)

<sup>‡</sup>PRISME, EDF R&D, 6 Quai Watier, 78400 Chatou, France and UMA, Inria, ENSTA Paris, Institut Polytechnique de Paris, 91120 Palaiseau, France. (lorenzo.audibert@edf.fr)

<sup>§</sup>Department of Mathematics, Virginia Tech, 24061 Blacksburg, USA. Corresponding author. (sgl22@vt.edu)

network model called SwitchNet. In a continuous setting, the low-rank structure was explored by [31] which focused on the theoretical basis for the low-rank structure and proved an explicit stability estimate (of Hölder-logarithmic type) for contrast in standard Sobolev spaces. We mention that the idea of low-rank structures can also be extended to other inverse problems such as the multi-frequency inverse source problem [19] and [3].

The low-rank structure of [26] is based on the discrete Fourier transform and ideas of butterfly algorithm; see also a theoretical analysis of a butterfly-net in [29]. The low-rank structure of [31] was based on the prolate spheroidal wave functions and their generalizations. These special functions were studied in a series of work [40, 41, 42] and we refer to the prolate spheroidal wave functions in two dimensions as disk PSWFs for convenience. One of the remarkable properties of the disk PSWFs is the so-called dual property: the disk PSWFs are the eigenfunctions of a restricted Fourier integral operator and of a Sturm-Liouville operator at the same time. It is this important dual property that leads to nontrivial and robust numerical algorithms, see [37] for a comprehensive introduction to the one dimensional PSWFs. For more recent studies on multidimensional generalizations of the PSWFs, we refer to [18, 39, 45] and the references therein.

In this work we demonstrate how to tackle the inverse scattering problem based on the low-rank structure given by the disk prolate spheroidal wave functions. The switchNet [26] perhaps has broader applications, and our low-rank structure is tailored for the inverse scattering problem. We first explore the idea based on the linearized or Born Model. Then our method being data-centric meaning that its implementation is not impacted by the model, we show numerically by using the fully non-linear model that it is robust to linearization. There are several key ingredients in our algorithm: evaluation of the PSWFs eigensystems, data processing, dimensionality reduction of data, and low dimensional projection.

To evaluate the disk PSWFs eigensystem in two dimensions, we apply the ideas of [18, 45]. In particular we compute the disk PSWFs by the Sturm-Liouville eigenvalue problem: this is robust and accurate due to the well-known spectral methods [16]; it is completely different from directly computing the eigenfunction from a compact operator which is a much more challenging problem [36]. After the evaluation of the disk PSWFs, we then compute the prolate eigenvalues by the interplay between the Sturm-Liouville operator and the Fourier integral operator. More computational details may be found in [17, 18, 39, 45]. We next proceed to process the far-field data and solve the unknown in the low-rank space via a spectral cutoff regularization. This can be applied to both the Born far-field data and the full far-field data. We process the far-field data to obtain a data set in the unit disk: this mimics some idea of the convolutional neural network (see for instance [15]); however our key reason to process the data in this way is due to the underlying mathematical model. According to appropriate mock-quadrature nodes (which are related to the disk PSWFs) in the unit disk, we continue to extract a smaller set of data (or filtered data) from the data set (which can be large scale) in the unit disk. This idea is in similar spirit to the mock-Chebyshev nodes [6]. Using the post-processed data in the disk, we then obtain their projections onto the disk PSWFs whose corresponding prolate eigenvalues are larger than a spectral cutoff parameter. Such a low-rank structure is tailored for the inverse scattering problem.

To shed light on the potential of our algorithm, we have conducted various numerical experiments and have observed the following interesting features. First, the algorithm leads to improved resolution. We have numerically tested objects which are

separated less than half wavelength, and these objects can be clearly distinguished from the reconstruction. We point out that similar improved resolution was also reported in [24]. Second, the proposed algorithm is robust to both randomly added noises and modeling errors. For experiments with Born data, the performance of the algorithm remains good even when we add large random noises; for experiments with full data, we have tested our algorithm when the Born modeling error (computed according to [8]) is not small, and the performance is still very good. This demonstrates that our algorithm has great potential to facilitate more advanced algorithms for the fully nonlinear model. Third, the proposed algorithm has the potential to be more favorable than direct implementations of Matlab built-in fft and certain iterative methods. Our direct implementation of Matlab built-in fft requires that the wavenumber respects certain periodicity, which imposes more restrictions on the problem (which may be overcome by the fractional Fourier transform [25] that is beyond the scope of this paper) and leads to worse resolution for lower frequency in comparison to our algorithm. The iterative methods [8] usually depend on the choice of initial guess and is more computationally expensive than our proposed algorithm. Fourth, the algorithm numerically demonstrates the so-called increasing stability [22, 43] thanks to our proposed low-rank structure. This is because that the low-rank space spanned by the disk PSWFs is evaluated accurately by the corresponding Sturm-Liouville eigenvalue problem, instead of being evaluated by an eigenvalue problem for a compact operator (whose leading eigenvalues are numerically the same).

The remaining of the paper is organized as follows. In Section 2 we introduce the mathematical model of the inverse scattering problem. To solve the inverse scattering problem, we need several analytical and computational results of disk PSWFs which are discussed in Section 3. The algorithm based on low-rank structures is proposed in Section 4. Finally we conduct various numerical experiments in Section 5 to illustrate the potential of our algorithm.

**2. Mathematical model of inverse scattering.** In this section, we introduce the inverse medium scattering problem in  $\mathbb{R}^2$ . Let  $k > 0$  be the wave number. A plane wave takes the following form

$$e^{ikx \cdot \hat{\theta}}, \quad \hat{\theta} \in \mathbb{S} := \{x \in \mathbb{R}^2 : |x| = 1\},$$

where  $\hat{\theta}$  is the direction of propagation. Let  $\Omega \subset \mathbb{R}^2$  be an open and bounded set with Lipschitz boundary  $\partial\Omega$  such that  $\mathbb{R}^2 \setminus \overline{\Omega}$  is connected. To best illustrate the parameter identification theory, we let the real-valued function  $q(x) \in L^\infty(\mathbb{R}^2)$  be the contrast of the medium,  $q > -1$  on  $\Omega$  and  $q = 0$  on  $\mathbb{R}^2 \setminus \overline{\Omega}$  such that the support of the contrast is  $\Omega$ . The scattering due to a plane wave  $e^{ikx \cdot \hat{\theta}}$  is to find total wave field  $u^t(x; \hat{\theta}; k) = e^{ikx \cdot \hat{\theta}} + u^s(x; \hat{\theta}; k)$  belonging to  $H_{loc}^1(\mathbb{R}^2)$  such that

$$(2.1) \quad \Delta_x u^t(x; \hat{\theta}; k) + k^2(1 + q(x))u^t(x; \hat{\theta}; k) = 0 \text{ in } \mathbb{R}^2,$$

$$(2.2) \quad \lim_{r:=|x| \rightarrow \infty} r^{\frac{1}{2}} \left( \frac{\partial u^s(x; \hat{\theta}; k)}{\partial r} - iku^s(x; \hat{\theta}; k) \right) = 0,$$

where the last equation, i.e., the Sommerfeld radiation condition, holds uniformly for all directions (and a solution is called radiating if it satisfies this radiation condition). The scattered wave field is  $u^s(\cdot; \hat{\theta}; k)$ . The above scattering problem (2.1)–(2.2) is a special case of the more general problem where one looks for a radiating solution  $u^s \in H_{loc}^1(\mathbb{R}^2)$  to

$$(2.3) \quad \Delta u^s + k^2(1 + q)u^s = -k^2 q f,$$

where  $f \in L^\infty(\mathbb{R}^2)$ . Setting  $f(x) = e^{ikx \cdot \hat{\theta}}$  in (2.3) recovers (2.1)–(2.2). This model is referred to as the full model.

It is known that there exists a unique radiating solution to (2.3), cf. [12] and [28]. For example, the solution can be obtained with the help of the Lippmann-Schwinger integral equation,

$$u^s(x) - k^2 \int_{\Omega} \Phi(x, y) q(y) u^s(y) dy = k^2 \int_{\Omega} \Phi(x, y) q(y) f(y) dy, \quad x \in \mathbb{R}^2.$$

where  $\Phi(x, y)$  is the fundamental function for the Helmholtz equation given by

$$\Phi(x, y) := \frac{i}{4} H_0^{(1)}(k|x - y|) \quad x \neq y,$$

here  $H_0^{(1)}$  denotes the Hankel function of the first kind of order zero ([12]). From the asymptotic of the scattered wave field (c.f. [9])

$$(2.4) \quad u^s(x; \hat{\theta}; k) = \frac{e^{i\frac{\pi}{4}}}{\sqrt{8k\pi}} \frac{e^{ikr}}{\sqrt{r}} \left( u^\infty(\hat{x}; \hat{\theta}; k) + \mathcal{O}\left(\frac{1}{r}\right) \right) \quad \text{as } r = |x| \rightarrow \infty,$$

uniformly with respect to all directions  $\hat{x} := x/|x| \in \mathbb{S}$ , we arrive at  $u^\infty(\hat{x}; \hat{\theta}; k)$  which is known as the far-field data (pattern) with  $\hat{x} \in \mathbb{S}$  denoting the observation direction. The multi-static data at a fixed frequency are given by

$$(2.5) \quad \{u^\infty(\hat{x}; \hat{\theta}; k) : \hat{x} \in \mathbb{S}, \hat{\theta} \in \mathbb{S}\}.$$

The inverse scattering problem is to determine the contrast  $q$  from these far-field data. It is known that this two dimensional inverse scattering problem has a unique solution, see for instance [7]. In practical applications, we are usually given the discrete far-field data at a set of uniformly distributed directions

$$(2.6) \quad \{u^\infty(\hat{x}_m; \hat{\theta}_\ell; k) : m = 1, 2, \dots, N_1, \ell = 1, 2, \dots, N_2\}.$$

The linear sampling method [11] and factorization method [27] are shape identification methods that recognize the nonlinear nature. Recently it was shown in [28] that the eigenvalues of the data operator and these of its linearized version (i.e., Born data operator) decay in the same rate. The work [34] also shares a similar spirit on the connection between the ill-posedness of the fully nonlinear model and the Born model. Thus important insights may be drawn from the Born model and for later purposes we introduce the Born model. The Born approximation  $u_b^s(x; \hat{\theta}; k)$  is the unique radiating solution to the Born model

$$(2.7) \quad \Delta u_b^s + k^2 u_b^s = -k^2 q e^{ikx \cdot \hat{\theta}} \quad \text{in } \mathbb{R}^2.$$

From the asymptotic behavior

$$u_b^s(x; \hat{\theta}; k) = \frac{e^{i\frac{\pi}{4}}}{\sqrt{8k\pi}} \frac{e^{ikr}}{\sqrt{r}} \left( u_b^\infty(\hat{x}; \hat{\theta}; k) + \mathcal{O}\left(\frac{1}{r}\right) \right) \quad \text{as } r \rightarrow \infty,$$

we obtain the Born far-field pattern  $u_b^\infty(\hat{x}; \hat{\theta}; k)$ ,  $\hat{x} = x/|x| \in \mathbb{S}$ . One advantage of the Born far-field data is that we can directly obtain an explicit formula by

$$(2.8) \quad u_b^\infty(\hat{x}; \hat{\theta}; k) = k^2 \int_{\Omega} e^{-ik\hat{x} \cdot y} q(y) e^{iky \cdot \hat{\theta}} dy.$$

This formula play a key role in our method. If we identify  $p = \frac{\theta - \hat{x}}{2} \in B(0, 1)$  where  $B(0, 1)$  denotes the unit disk, then the knowledge of the multistatic Born far-field data gives the knowledge of the restricted Fourier transform of the unknown  $q$ , i.e.,  $\int_{\Omega} e^{icpy} q(y) dy$  for  $p \in B(0, 1)$ . It is known that the restricted Fourier integral operator has a low-rank structure, see for instance [41, 31] for the continuous case and [26] for the discrete case. In the following we show how to explore the low-rank structure to solve for our (linearized and nonlinear) inverse scattering problem.

**3. Generalization of prolate spheroidal wave functions.** The low-rank structure of our paper is based on the generalizations of prolate spheroidal wave functions (PSWFs). The PSWFs and their generalizations were studied in a series of work by Slepian [40, 41, 42]. For a comprehensive introduction to the one dimensional PSWFs, we refer to [37]. For more recent studies on multidimensional generalizations of the PSWFs, we refer to [18, 39, 45]. For our inverse problem, we rely on the generalization of PSWFs to two dimensions.

**3.1. Disk PSWFs.** According to [41], there exist real-valued eigenfunctions  $\{\psi_{m,n,l}(x; c)\}_{m,n \in \mathbb{N}}^{l \in \mathbb{I}(m)}$  of the restricted Fourier transform with bandwidth parameter  $c$ :

$$\begin{aligned} \mathcal{F}_{B(0,1)}^c \psi_{m,n,l}(x; c) &= \int_{B(0,1)} e^{icx \cdot y} \psi_{m,n,l}(y; c) dy \\ (3.1) \qquad \qquad \qquad &= \alpha_{m,n}(c) \psi_{m,n,l}(x; c), \quad x \in B(0, 1), \end{aligned}$$

where  $\mathbb{N} = \{0, 1, 2, 3, \dots\}$  and

$$\mathbb{I}(m) = \begin{cases} \{1\} & m = 0 \\ \{1, 2\} & m \geq 1 \end{cases}.$$

For notation convenience, we refer to  $\psi_{m,n,l}(x; c)$  as the disk PSWFs and  $\alpha_{m,n}(c)$  as the prolate eigenvalues in this paper.

One important property of the disk PSWFs is the so-called dual property. [41] gave the Sturm-Liouville problem for the radial part and one can show by a direct calculation that the disk PSWFs are also eigenfunctions of a Sturm-Liouville operator, i.e.,

$$(3.2) \qquad \mathcal{D}_c[\psi_{m,n,l}](x) = \chi_{m,n} \psi_{m,n,l}(x), \quad x \in B(0, 1),$$

where

$$\mathcal{D}_c := -(1 - r^2) \partial_r^2 - \frac{1}{r} \partial_r + 3r \partial_r - \frac{1}{r^2} \Delta_0 + c^2 r^2$$

and the Laplace–Beltrami operator  $\Delta_0 = \partial_{\theta}^2$  is the spherical part of Laplacian  $\Delta$ . More details can be found in [31] and [45]. We refer to  $\chi_{m,n}(c)$  as the Sturm-Liouville eigenvalue.

We briefly state the following properties of disk PSWFs and refer to [41] and [45] for a proof.

**LEMMA 3.1.** *For any  $c > 0$ ,  $\{\psi_{m,n,l}(x; c)\}_{m,n \in \mathbb{N}}^{l \in \mathbb{I}(m)}$  forms a complete and orthonormal system of  $L^2(B(0, 1))$ , i.e., for  $\forall m, n, m', n' \in \mathbb{N}, l \in \mathbb{I}(m), l' \in \mathbb{I}(m')$  it holds that*

$$\int_{B(0,1)} \psi_{m,n,l}(y; c) \psi_{m',n',l'}(y; c) dy = \delta_{mm'} \delta_{nn'} \delta_{ll'},$$

where  $\delta$  denotes the Kronecker delta. The corresponding Sturm-Liouville eigenvalues  $\{\chi_{m,n}\}_{m,n \in \mathbb{N}}$  in (3.2) are real positive which are ordered for fixed  $m$  as follows

$$0 < \chi_{m,0}(c) < \chi_{m,1}(c) < \chi_{m,2}(c) < \cdots .$$

LEMMA 3.2. For any  $c > 0$ , every prolate eigenvalue  $\alpha_{m,n}(c)$  is non-zero, and  $\lambda_{m,n} = |\alpha_{m,n}(c)|$  can be arranged for fixed  $m$  as

$$\lambda_{m,n_1}(c) > \lambda_{m,n_2}(c) > 0, \quad \forall n_1 < n_2.$$

Moreover  $\lambda_{m,n}(c) \rightarrow 0$  as  $m, n \rightarrow +\infty$ .

Lemma 3.2 states that the restricted Fourier integral operator has a low-rank structure. More importantly, Lemma 3.1 states that the computation of the disk PSWFs can be done using the Sturm-Liouville operator so that it is extremely stable and efficient. The disk PSWFs serve as an important tool to solve the two-dimensional inverse scattering problem. We next illustrate their computations and relevant quadrature in order to propose the algorithm. For a theoretical analysis of disk PSWFs with application to inverse scattering, we refer to [31].

**3.2. Evaluation of disk PSWFs and prolate eigenvalues.** Using polar coordinates, each disk PSWF  $\psi_{m,n,l}(x; c)$  can be obtained by separation of variables by (cf. [41] or [31])

$$\psi_{m,n,l}(x; c) = r^m \varphi_{m,n}(2\|x\|^2 - 1; c) Y_{m,l}(\hat{x}), \quad x \in B(0, 1),$$

where  $x = r\hat{x} = (r \cos \theta, r \sin \theta)^T$  and the spherical harmonics  $Y_{m,l}(\hat{x})$  is given by

$$(3.3) \quad Y_{m,l}(\hat{x}) = \begin{cases} \frac{1}{\sqrt{2\pi}}, & m = 0, l = 1 \\ \frac{1}{\sqrt{\pi}} \cos m\theta, & m \geq 1, l = 1 \\ \frac{1}{\sqrt{\pi}} \sin m\theta, & m \geq 1, l = 2 \end{cases} .$$

An efficient method to evaluate the disk PSWFs is to expand  $\varphi_{m,n}(\eta; c)$  by normalized Jacobi polynomials  $\{P_j^{(m)}(\eta)\}_{\eta \in (-1,1)}$ ,

$$(3.4) \quad \varphi_{m,n}(\eta; c) = \sum_{j=0}^{\infty} \beta_j^{m,n}(c) P_j^{(m)}(\eta).$$

In the following section, with reference to [45] we will discuss the evaluation of the coefficients  $\{\beta_j^{m,n}(c)\}$  and use them to determine the prolate eigenvalues.

**3.2.1. Jacobi polynomials.** We introduce the normalized Jacobi polynomials  $\{P_n^{(\alpha,\beta)}(\eta)\}_{\eta \in (-1,1)}$  which are eigenfunctions of the following Sturm-Liouville problem,

$$(3.5) \quad -\frac{1}{w_{\alpha,\beta}(\eta)} \partial_\eta \left( w_{\alpha+1,\beta+1}(\eta) \partial_\eta P_n^{(\alpha,\beta)}(\eta) \right) = n(n + \alpha + \beta + 1) P_n^{(\alpha,\beta)}(\eta)$$

where  $w_{\alpha,\beta}(\eta) = (1 - \eta)^\alpha (1 + \eta)^\beta$ , and they satisfy the orthogonality condition

$$(3.6) \quad \int_{-1}^1 P_n^{(\alpha,\beta)}(\eta) P_{n'}^{(\alpha,\beta)}(\eta) d\eta = 2^{\alpha+\beta+2} \delta_{nn'}, \quad \forall n, n' \in \mathbb{N}.$$

In this paper we work with  $\alpha = 0$  and  $\beta = m$ . Hence we write, without the danger of confusion,  $P_n^{(m)} = P_n^{(0,m)}$ .

The normalized Jacobi polynomials  $\{P_n^{(m)}(x)\}_{x \in (-1,1)}$  can be obtained through the three-term recurrence relation

$$\begin{aligned} P_{n+1}^{(m)}(x) &= \frac{1}{a_n} [(x - b_n)P_n^{(m)}(x) - a_{n-1}P_{n-1}^{(m)}(x)], \quad n \geq 1 \\ P_0^{(m)}(x) &= \frac{1}{h_0}, \quad P_1^{(m)}(x) = \frac{1}{2h_1} [(m+2)x - m] \end{aligned}$$

where

$$(3.7) \quad \begin{cases} a_n = \frac{2(n+1)(n+m+1)}{(2n+m+2)\sqrt{(2n+\beta+1)(2n+m+3)}} \\ b_n = \frac{m^2}{(2n+m)(2n+m+2)} \\ h_n = \frac{1}{\sqrt{2(2n+m+1)}} \end{cases}, \quad n \in \mathbb{N}.$$

For a more comprehensive introduction to special polynomials, we refer to [1].

**3.2.2. Approximation of disk PSWFs system.** To compute the coefficients of (3.4), we plug this expansion into (3.2) and we can derive (by noting (3.5) and the fact that  $\Delta_0 Y_{m,l}(\hat{x}) = -m^2 Y_{m,l}(\hat{x})$ , or by [45]) that the coefficients  $\{\beta_j^{m,n}\}_{j \in \mathbb{N}}$  satisfy

$$(3.8) \quad \begin{aligned} \left( \gamma_{m+2j} + \frac{(1+b_j)c^2}{2} - \chi_{m,n}(c) \right) \beta_j^{m,n} \\ + \frac{a_{j-1}c^2}{2} \beta_{j-1}^{m,n} + \frac{a_j c^2}{2} \beta_{j+1}^{m,n} = 0, \quad j \geq 0 \end{aligned}$$

where  $\gamma_{m+2j} = (m+2j)(m+2j+2)$ . Here  $\chi_{m,n}(c)$  is the Sturm-Liouville eigenvalue.

To evaluate eigensystem  $\{\psi_{m,n,l}(x; c), \chi_{m,n}\}$  for  $2n+m \leq N$ , we follow [45] to set  $\tilde{M} = 2N + 30$  and obtain the approximations  $\{\tilde{\psi}_{m,n,l}(x; c), \tilde{\chi}_{m,n}\}$  by

$$(3.9) \quad \tilde{\psi}_{m,n,l}(x; c) = \sum_{j=0}^K \tilde{\beta}_j^{m,n} \|x\|^m P_j^{(m)}(2\|x\|^2 - 1) Y_{m,l}(\hat{x}), \quad 2n+m \leq N$$

where  $K = \lceil \frac{\tilde{M}-m}{2} \rceil$ . As such,  $\{\tilde{\beta}_j^{m,n}\}$  and  $\tilde{\chi}_{m,n}$  can be solved from the following tridiagonal linear system

$$(3.10) \quad A \tilde{\beta}^{m,n} = \tilde{\chi}_{m,n} \tilde{\beta}^{m,n}$$

where  $\tilde{\beta}^{m,n} = (\tilde{\beta}_0^{m,n}, \tilde{\beta}_1^{m,n}, \dots, \tilde{\beta}_K^{m,n})^T$ ,  $A$  is a  $(K+1) \times (K+1)$  symmetric tridiagonal matrix whose nonzero entries are given by

$$\begin{aligned} A_{j,j} &= \gamma_{m+2j} + \frac{(1+b_j)c^2}{2}, \\ A_{j,j+1} &= A_{j+1,j} = \frac{a_j c^2}{2}, \quad j \geq 0. \end{aligned}$$

Since  $\|\psi_{m,n,l}(x; c)\|_{L^2(B(0,1))} = 1$ , the coefficient vector  $\tilde{\beta}^{m,n}$  are normalized to satisfy

$$\|\tilde{\beta}^{m,n}\|_2 = \sqrt{\sum_{j=0}^K |\tilde{\beta}_j^{m,n}|^2} = 1$$

owing to  $\|P_{m,j,l}\|_{L^2(B(0,1))} = 1$  where  $P_{m,j,l}(x) = \|x\|^m P_j^{(m)}(2\|x\|^2 - 1)Y_{m,l}(\hat{x})$ . We further sort the eigenvalues by

$$\tilde{\chi}_{m,j} < \tilde{\chi}_{m,i}, \quad j < i.$$

Finally to evaluate the prolate eigenvalues  $\{\alpha_{m,n}\}_{m,n \in \mathbb{N}}$ , the following formula was given in [45]

$$(3.11) \quad \tilde{\alpha}_{m,n}(c) = i^m \tilde{\lambda}_{m,n}(c), \quad \tilde{\lambda}_{m,n}(c) = \frac{\pi c^m}{2^{m-\frac{1}{2}} m! \sqrt{m+1}} \frac{\tilde{\beta}_0^{m,n}}{\tilde{\varphi}_{m,n}(-1; c)}$$

where  $\tilde{\varphi}_{m,n}(-1; c) = \sum_{j=0}^K \tilde{\beta}_j^{m,n} P_j^{(m)}(-1)$ . This formula is sufficient for our inverse problem.

We summarize the following algorithm for the evaluation of PSWFs and prolate eigenvalues.

---

**Algorithm 3.1** Evaluation of PSWF and prolate eigenvalue

---

**Require:** Parameter  $c$ , index of disk PSWF  $(m, n, l)$  and  $x \in \mathbb{R}^2$ .

**Ensure:**  $\psi_{m,n,l}(x; c)$  and prolate eigenvalue  $\alpha_{m,n}(c)$ .

- 1: Compute the tridiagonal linear system Equation (3.10) (and sort the eigenvalues from small to large) to obtain the eigenvector  $\tilde{\beta}^{m,n}$  and the eigenvalue  $\tilde{\chi}_{m,n}(c)$  corresponding to the given  $(m, n)$ . Here  $\tilde{\beta}^{m,n} = (\tilde{\beta}_0^{m,n}, \tilde{\beta}_1^{m,n}, \dots, \tilde{\beta}_K^{m,n})^T$ .
  - 2: Evaluate  $(P_{m,0}(2\|x\|^2 - 1), P_{m,1}(2\|x\|^2 - 1), \dots, P_{m,K}(2\|x\|^2 - 1))^T$  at  $x \in \mathbb{R}^2$  by the recurrence (3.7) and the spherical harmonics  $Y_{m,l}(\hat{x})$  at  $\hat{x}$  by Equation (3.3).
  - 3: Compute the approximation of disk PSWFs by  $\tilde{\psi}_{m,n,l}(x; c) = \|x\|^m Y_{m,l}(\hat{x}) \sum_{j=0}^K \tilde{\beta}_j^{m,n} P_j^{(m)}(2\|x\|^2 - 1)$ .
  - 4: Evaluate the prolate eigenvalue  $\tilde{\alpha}_{m,n}(c) = i^m \tilde{\lambda}_{m,n}(c)$  according to Equation (3.11).
- 

**3.3. Quadrature.** Later on, we need to project our data onto the disk PSWFs. This motivates us to consider an appropriate quadrature for the projection (i.e. integral). In the remaining of this section, we simply identify  $w(x)$  as  $w(r, \theta)$  where  $(r, \theta)$  is the polar representation of  $x$ . Here we employ a Gauss-Legendre quadrature rule for the radial part and a trapezoidal quadrature rule for the angular part to obtain, for any function  $w \in L^2(B(0, 1))$

$$\begin{aligned} w_{m,n,l} &= \int_{B(0,1)} w(x) \psi_{m,n,l}(x) dx = \int_0^{2\pi} \int_0^1 w(r, \theta) \psi_{m,n,l}(r, \theta) r dr d\theta \\ &\quad (\text{change of variable } t = 2r^2 - 1) \\ &= \frac{1}{4} \int_0^{2\pi} \int_{-1}^1 w(\sqrt{(1+t)/2}, \theta) \psi_{m,n,l}(\sqrt{(1+t)/2}, \theta) dt d\theta \\ &\approx \frac{1}{4} \sum_{i=0}^{M-1} \sum_{j=0}^{T-1} w(\sqrt{(1+t_j)/2}, \theta_i) \psi_{m,n,l}(\sqrt{(1+t_j)/2}, \theta_i) \omega_{t_j} \omega_{\theta_i}, \end{aligned}$$

where

$$(3.12) \quad \left\{ t_j, \omega_{t_j} \right\}_{j=0}^{T-1} : \text{Gauss-Legendre quadrature nodes and weights,} \\ \left\{ \theta_i = \frac{2i\pi}{M}, \omega_{\theta_i} = \frac{2\pi}{M} \right\}_{i=0}^{M-1} : \text{trapezoidal quadrature nodes and weights.}$$

We point out that it is possible to make more use of the disk PSWFs to investigate other quadratures depending on the parameter  $c$ , see for instance in the one dimensional case [37]; we choose to use the above quadrature independent of the parameter  $c$  (i.e. independent of the wavenumber  $k$ ) which fits our inverse scattering problem.

Suppose that the data are projected onto a low-rank space  $\{\psi_{m,n,\ell}\}_{(m,n,\ell) \in J_\epsilon}$  with  $J_\epsilon := \{(m,n,\ell) : |\alpha_{m,n}| > \epsilon\}$ . With the above quadrature and polynomial approximation error estimate [17], one way to choose the number of quadrature nodes  $TM$  is given by

$$(3.13) \quad T = \max \{T(m,m',n,n') : \exists l \in \{1,2\}, \text{ s.t.}, (m,n,l), (m',n',l') \in J_\epsilon\},$$

and

$$(3.14) \quad M = 2m_{\max} + 1, \quad m_{\max} = \max\{m : \exists l \in \{1,2\}, \text{ s.t.}, (m,n,l) \in J_\epsilon\},$$

for the given  $J_\epsilon$ ; here

$$T(m,m',n,n') = \lceil \frac{1}{2} \left( \frac{m+m'+2}{2} + K(m,n) + K(m',n') \right) \rceil,$$

and

$$K(m,n) = \lceil \frac{1}{2} \left( \log_{\frac{1}{2}} \left( \frac{\gamma\epsilon}{\pi} \right) - m + \frac{1}{2} \right) \rceil.$$

for a very small parameter  $\gamma = 0.05$ .

**4. A method based on the low-rank structure.** Now we are ready to elaborate our proposed method based on the low-rank structure for the inverse scattering problem. The two main ingredients are data processing and low dimensional projection.

**4.1. Data processing.** For the inverse scattering problem, we work with the far-field data which are given by (2.6), i.e.,

$$\{u^\infty(\hat{x}_m; \hat{\theta}_\ell; k) : m = 1, 2, \dots, N_1, \ell = 1, 2, \dots, N_2\},$$

where both  $\{\hat{x}_m\}_{m=1}^{N_1}$  and  $\{\hat{\theta}_\ell\}_{\ell=1}^{N_2}$  are uniformly distributed directions. We first apply the transformation

$$(\hat{x}_m, \hat{\theta}_\ell) \mapsto \frac{\hat{\theta}_\ell - \hat{x}_m}{2}$$

to transform the datum  $u^\infty(\hat{x}_m; \hat{\theta}_\ell; k)$  on  $S \times S$  to an equivalent datum evaluated at  $\frac{\hat{\theta}_\ell - \hat{x}_m}{2} \in B = B(0, 1)$ , particularly we identify

$$u(p_{m\ell}; c) = \frac{1}{k^2} u^\infty(\hat{x}_m; \hat{\theta}_\ell; k), \quad p_{m\ell} = \frac{\hat{\theta}_\ell - \hat{x}_m}{2}, \quad c = 2k.$$

The new data set  $\{u(p_{m\ell}; c) : m = 1, 2, \dots, N_1, \ell = 1, 2, \dots, N_2\}$  is of dimension  $N_1 N_2$ . We continue to extract a set of data from the data set  $\{u(p_{m\ell}; c) : m = 1, 2, \dots, N_1, \ell = 1, 2, \dots, N_2\}$  (which can be large scale). Particularly, the subset  $\{u(\tilde{p}_n; c) : n = 1, 2, \dots, TM\}$  will be extracted, where  $\{\tilde{p}_n\}_{n=1}^{TM}$  are mock-quadrature nodes that are approximations to the exact quadrature nodes  $\{p_n\}_{n=1}^{TM}$  in  $B$ . Here we identify  $\{p_n\}_{n=1}^{TM}$  with  $\left\{ \sqrt{\frac{t_j+1}{2}} (\cos \theta_i, \sin \theta_i)^T \right\}_{j=0, i=0}^{T-1, M-1}$  where the exact quadrature nodes are given by (3.12). This idea is in similar spirit to the mock-Chebyshev nodes [6].

The extraction of the approximate or mock-quadrature nodes is as follows. Given exact quadrature nodes  $\{p_n\}_{n=1}^{T \times M}$  and far-field data at the uniformly distributed directions  $\{\hat{x}_m, \hat{\theta}_\ell : m = 1, 2, \dots, N_1, \ell = 1, 2, \dots, N_2\}$ , the approximate or mock-quadrature nodes  $\{\tilde{p}_n\}_{n=1}^{T \times M}$  are given by

$$\tilde{p}_n = \frac{\hat{\theta}_{\ell^*} - \hat{x}_{j^*}}{2} \quad \text{where} \quad (\ell^*, j^*) = \operatorname{argmin}_{\ell, j} \left\| p_n - \frac{\hat{\theta}_\ell - \hat{x}_j}{2} \right\|_2.$$

We summarize the data extraction algorithm in Algorithm 4.1. Figure 1 shows the exact quadrature nodes in (a), the  $N_1 \times N_2 = 100 \times 100$  grid nodes before dimensionality reduction in (b), and the mock-quadrature nodes in (c).

Given  $\{\tilde{p}_n\}_{n=1}^{TM}$ , we obtain its equivalent set in polar coordinates given by  $\left\{ \sqrt{\frac{\tilde{t}_j+1}{2}} (\cos \tilde{\theta}_i, \sin \tilde{\theta}_i)^T \right\}_{j=0, i=0}^{T-1, M-1}$  and set  $\{\tilde{u}(\tilde{t}_j, \tilde{\theta}_i; c)\}_{j=0, i=0}^{T-1, M-1} = \{u(\tilde{p}_n; c)\}_{n=1}^{TM}$ .

We define the post-processed data (and we also refer to its continuous counterpart as the post-processed data without danger of confusion) by

$$(4.1) \quad U = \begin{pmatrix} \tilde{u}(\tilde{t}_0, \tilde{\theta}_0; c) & \tilde{u}(\tilde{t}_0, \tilde{\theta}_1; c) & \cdots & \tilde{u}(\tilde{t}_0, \tilde{\theta}_{M-1}; c) \\ \tilde{u}(\tilde{t}_1, \tilde{\theta}_0; c) & \tilde{u}(\tilde{t}_1, \tilde{\theta}_1; c) & \cdots & \tilde{u}(\tilde{t}_1, \tilde{\theta}_{M-1}; c) \\ \vdots & \vdots & \ddots & \vdots \\ \tilde{u}(\tilde{t}_{T-1}, \tilde{\theta}_0; c) & \tilde{u}(\tilde{t}_{T-1}, \tilde{\theta}_1; c) & \cdots & \tilde{u}(\tilde{t}_{T-1}, \tilde{\theta}_{M-1}; c) \end{pmatrix}.$$

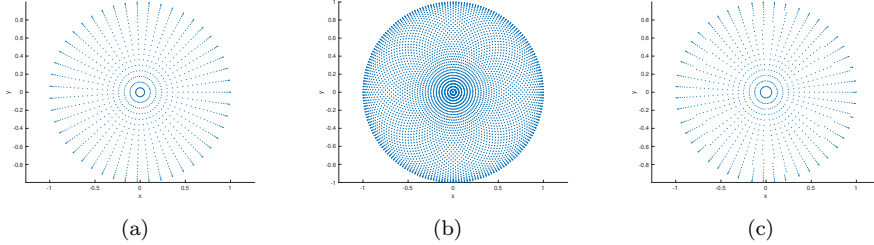


Fig. 1: (a) exact quadrature nodes with  $T = 24, M = 47$ . (b)  $N_1 \times N_2 = 100 \times 100$  grid nodes before dimensionality reduction. (c) approximate or mock-quadrature nodes.

**4.2. Solution in low-rank space and spectral cutoff regularization.** In this section, we suppose that we are given the matrix  $U = (U_{ji})$  with  $j = 0, 1 \dots T-1$  and  $i = 0, 1, \dots, M-1$  defined by (4.1). Our goal is to project these data onto a low-rank space spanned by the disk PSWFs.

To begin with, consider the post-processed problem to determine the unknown  $q \in L^2(B(0, 1))$  from the post-processed data  $u(x; c)$  by

$$(4.2) \quad u(x; c) = \int_{B(0,1)} e^{icx \cdot y} q(y) dy, \quad x \in B(0, 1),$$

where  $c > 0$  is the parameter given by  $c = 2k$ .

---

**Algorithm 4.1** Data Processing
 

---

**Require:** far-field data  $\{u^\infty(\hat{x}_m; \hat{\theta}_\ell; k) : m = 1, 2, \dots, N_1, \ell = 1, 2, \dots, N_2\}$

**Ensure:** Post-processed data  $U$

- 1: Compute Gauss-Legendre quadrature nodes and weights  $\{t_j, \omega_{t_j}\}_{j=0}^{T-1}$ , and trapezoidal quadrature nodes and weights  $\{\theta_i = \frac{2i\pi}{M}, \omega_{\theta_i} = \frac{2\pi}{M}\}_{i=0}^{M-1}$ . Identify  $\{p_n\}_{n=1}^{TM}$  with  $\{\sqrt{\frac{t_j+1}{2}}(\cos \theta_i, \sin \theta_i)^T\}_{j=0, i=0}^{T-1, M-1}$ .
  - 2: Find  $(\ell^*, m^*)$  such that  $(\ell^*, m^*) = \operatorname{argmin}_{\ell, m} \|p_n - \frac{\hat{\theta}_\ell - \hat{x}_m}{2}\|_2$
  - 3: Compute approximate or mock-quadrature nodes  $\tilde{p}_n = \frac{\hat{\theta}_{\ell^*} - \hat{x}_{m^*}}{2}$  for  $n = 1, 2, \dots, TM$ . Identify  $\{\tilde{p}_n\}_{n=1}^{TM}$  with  $\{\sqrt{\frac{t_j+1}{2}}(\cos \tilde{\theta}_i, \sin \tilde{\theta}_i)^T\}_{j=0, i=0}^{T-1, M-1}$ .
  - 4: Evaluate the post-processed data  $u(\tilde{p}_n) = \frac{1}{k^2} u^\infty(\hat{x}_{m^*}, \hat{\theta}_{\ell^*}; k)$ .
  - 5: Formulate the matrix  $U_{ji} = u(\tilde{p}_n)$  by identifying  $\{n : 1 \leq n \leq TM\}$  with  $\{(j, i) : j = 0, 1 \dots T-1, i = 0, 1, \dots, M-1\}$ .
- 

---

**Algorithm 4.2** Low Dimensional Projection
 

---

**Require:** Matrix  $U = (U_{ji})_{j=0, 1 \dots T-1, i=0, 1, \dots, M-1}$  defined by (4.1), spectral cutoff regularization parameter  $\epsilon$

**Ensure:** The low dimensional vector  $\{q_{m,n,\ell}\}_{(m,n,\ell) \in J_\epsilon}$  with  $J_\epsilon := \{(m, n, \ell) : |\alpha_{m,n}| > \epsilon\}$

- 1: For all  $(m, n, \ell) \in J_\epsilon$ , apply the quadrature to compute

$$u_{m,n,\ell} \approx \frac{1}{4} \sum_{i=0}^{M-1} \sum_{j=0}^{T-1} U_{ji} \psi_{m,n,\ell}(\sqrt{(1+t_j)/2}, \theta_i) \omega_{t_j} \omega_{\theta_i},$$

where  $\{t_j, \omega_{t_j}\}_{j=0}^{T-1}$  and  $\{\theta_i = \frac{2i\pi}{M}, \omega_{\theta_i} = \frac{2\pi}{M}\}_{i=0}^{M-1}$  are quadrature nodes and weights given by (3.12).

- 2: Compute  $q_{m,n,\ell} = \frac{u_{m,n,\ell}}{\alpha_{m,n}}$  for all  $(m, n, \ell) \in J_\epsilon$ .
- 

Given the disk PSWFs  $\{\psi_{m,n,\ell}\}_{m,n \in \mathbb{N}}^{l \in \mathbb{I}(m)}$  which form a complete and orthonormal basis of  $L^2(B)$ , we expand the unknown function  $q$  and post-processed data  $u$  in a series,

$$q(x) = \sum_{m,n \in \mathbb{N}, l \in \mathbb{I}(m)} q_{m,n,\ell} \psi_{m,n,\ell}(x; c), \quad u(x; c) = \sum_{m,n \in \mathbb{N}, l \in \mathbb{I}(m)} u_{m,n,\ell} \psi_{m,n,\ell}(x; c)$$

where  $u_{m,n,\ell}$  and  $q_{m,n,\ell}$  are the projections of  $u(x; c)$  and  $q(x)$  on each  $\psi_{m,n,\ell}(x; c)$  respectively, i.e.,

$$u_{m,n,\ell} = \langle u(\cdot; c), \psi_{m,n,\ell}(\cdot; c) \rangle, \quad q_{m,n,\ell} = \langle q, \psi_{m,n,\ell}(\cdot; c) \rangle,$$

here  $\langle \cdot, \cdot \rangle$  denotes the  $L^2(B)$  inner product. From the property (3.1), one directly find that

$$q_{m,n,\ell} = \frac{u_{m,n,\ell}}{\alpha_{m,n}}.$$

The prolate eigenvalues  $\alpha_{m,n}$  decay to zero exponentially fast and the dominant prolate eigenvalues are numerically the same. See Figure 2 for an illustra-

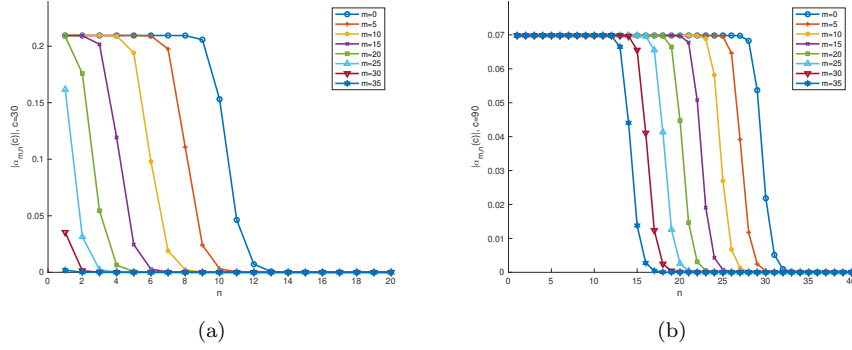


Fig. 2: Distributions of the absolute value of eigenvalues  $\alpha_{m,n}(c)$  for  $m = 0, 5, 10, 15, 20, 25, 30, 35$ . (a)  $c = 30$ , (b)  $c = 90$ .

tion. Therefore we can choose the spectral cutoff regularization parameter according to the noises or perturbation errors. The strategy to choose the regularization parameter will be discussed in detail in the numerical experiments. Recall that  $J_\epsilon = \{(m, n, \ell) : |\alpha_{m,n}| > \epsilon\}$ , we apply the spectral cutoff regularization to obtain that

$$\tilde{q}^\epsilon(x) = \sum_{(m,n,\ell) \in J_\epsilon} q_{m,n,\ell} \psi_{m,n,\ell}(x; c).$$

We summarize the low-dimensional projection in Algorithm 4.2.

**4.3. Method based on the low-rank structure.** In this section, we summarize our method in Algorithm 4.3. Given far-field data  $\{u^\infty(\hat{x}_m; \hat{\theta}_\ell; k) : m = 1, 2, \dots, N_1, \ell = 1, 2, \dots, N_2\}$ , we first apply Algorithm 4.1 to obtain the matrix  $U = (U_{ji})$  with  $j = 0, 1, \dots, T-1$  and  $i = 0, 1, \dots, M-1$ , then we apply Algorithm 4.2 to compute the coefficients  $\{u_{m,n,l}\}$  and  $\{q_{m,n,l}\}$ . This allows us to reconstruct the unknown  $q$ .

For completeness we discuss the mathematical theory that supports our method. In particular, suppose  $u^\delta$  is a perturbation of  $u$  in (4.2) such that  $\|u^\delta - u\|_{L^2(B)} \leq \delta$ . Let

$$q^{\delta,\alpha} = \sum_{\chi_{m,n}(c) < \alpha^{-1}} \frac{1}{\alpha_{m,n}(c)} \langle u^\delta, \psi_{m,n,\ell}(\cdot; c) \rangle_B \psi_{m,n,\ell}(\cdot; c),$$

and  $\beta(\alpha) = \min_{\chi_{m,n}(c) < \alpha^{-1}} \{|\alpha_{m,n}(c)|\}$ . Then the following follows from [31].

LEMMA 4.1. *Let  $\|u^\delta - u\|_{L^2(B)} \leq \delta$ . If  $q \in H^s(B)$  with  $0 < s < 1/2$ , then*

$$\|q^{\delta,\alpha} - q\|_{L^2(B)} \leq \frac{\delta}{\beta(\alpha)} + (4\alpha C)^{s/2} (1 + c^2)^{s/2} \|q\|_{H^s(B)},$$

where  $C \geq \sqrt{3}$  is a positive constant independent of  $\delta$ ,  $\alpha$ ,  $s$  and  $c$ .

The first error term  $\frac{\delta}{\beta(\alpha)}$  is primarily due to the perturbation noises, and the second error term  $(4\alpha C)^{s/2} (1 + c^2)^{s/2} \|q\|_{H^s(B)}$  is due to truncation error of finite prolate

series expansion of  $q$ . In particular, if  $q$  belongs to the span of finitely many disk PSWFs, then the stability estimate is of Lipschitz. We can prove the following.

**THEOREM 4.2.** *Let  $\|u^\delta - u\|_{L^2(B)} \leq \delta$ . If  $q \in \text{span}\{\psi_{m,n,\ell}(\cdot; c) : \alpha_{m,n} > \eta\}$ , then*

$$\|q^{\delta,\alpha} - q\|_{L^2(B)} \leq \frac{\delta}{\eta}.$$

*Proof.* Due to the assumption that  $q \in \text{span}\{\psi_{m,n,\ell}(\cdot; c) : \alpha_{m,n} > \eta\}$ , then

$$\|q^{\delta,\alpha} - q\|_{L^2(B)} \leq \frac{1}{\min\{\alpha_{m,n} : \alpha_{m,n} > \eta\}} \|u^\delta - u\|_{L^2(B)} < \frac{\delta}{\eta}.$$

This completes the proof.  $\square$

---

**Algorithm 4.3** low-rank InvScatt

---

**Require:** far-field data  $\{u^\infty(\hat{x}_m; \hat{\theta}_\ell; k) : m = 1, 2, \dots, N_1, \ell = 1, 2, \dots, N_2\}$ , spectral cutoff parameter  $\epsilon$

**Ensure:** Reconstruction  $\tilde{q}^\epsilon$  of the unknown  $q$

- 1: Precomputing: set  $c = 2k$ , apply Algorithm 3.1 to evaluate  $\psi_{m,n,l}(x; c)$  and prolate eigenvalue  $\alpha_{m,n}(c)$ .
  - 2: Dimensionality reduction of data: apply Algorithm 4.1 to obtain the matrix  $U$  given by (4.1).
  - 3: Low dimensional projection: apply Algorithm 4.2 to obtain the low dimensional vector  $\{q_{m,n,\ell}\}_{(m,n,\ell) \in J_\epsilon}$  with  $J_\epsilon := \{(m, n, \ell) : \alpha_{m,n}(c) > \epsilon\}$ .
  - 4: Evaluate  $\tilde{q}^\epsilon(x) = \sum_{(m,n,\ell) \in J_\epsilon} q_{m,n,\ell} \psi_{m,n,l}(x; c)$ .
- 

**5. Numerical experiments.** In this section, we perform numerical experiments for both the Born far-field data and the full far-field data. We aim to test resolution capability, robustness against randomly added noise and modeling errors, and numerical evidence of increasing stability. Furthermore, we compare its performance against standard fft and iterative methods.

**5.1. Born model.** We begin with the Born far-field data. Recall from the Born model (2.8) that

$$u_b^\infty(\hat{x}; \hat{\theta}; k) = k^2 \int_{\Omega} e^{-ik\hat{x}\cdot y} q(y) e^{ik y \cdot \hat{\theta}} dy.$$

One finds that

$$u_b^\infty(\hat{x}; \hat{\theta}; k) = k^2 \int_B e^{ic \frac{\hat{\theta} - \hat{x}}{2} \cdot y} q(y) dy,$$

and we set

$$(5.1) \quad u(p; c) = \int_B e^{icp \cdot y} q(y) dy, \quad p = \frac{\hat{\theta} - \hat{x}}{2}, \quad c = 2k.$$

**5.1.1. Data generation.** In this section, we discuss the Born data generated in our algorithm. We generate the far-field data by evaluating the integral (5.1) analytically (by hand), which avoids any possibility of inverse crimes. We consider the following unknowns.

- Eigenfunction. Let  $q(x) = \psi_{m,n,l}(x)$  be one of the eigenfunctions, then  $u(x; c) = \alpha_{m,n}(c)\psi_{m,n,l}(x)$ .
- Constant  $q$  in a disk/rectangle.
  - Constant in a disk:  $q(x) = 1_{|x| < a}(x)$ . This leads to

$$u(x; c) = \frac{2\pi a}{c|x|} J_1(ac|x|),$$

where  $J_1$  is the Bessel function of the first kind of order  $\nu = 1$ , see for instance [1].

- Constant in a rectangle:  $q(x) = 1_{x \in \Omega}(x)$ ,  $\Omega = \{x \in \mathbb{R}^2 : |x_1|, |x_2| < 1/2\}$ . This leads to

$$u(x; c) = \frac{4 \sin(\frac{c}{2}x_1) \sin(\frac{c}{2}x_2)}{c^2 x_1 x_2}.$$

- Oscillatory contrast:  $q(x_1, x_2) = \sin m\pi x_1 \cdot 1_{\Omega}(x)$ ,  $\Omega = \{x \in \mathbb{R}^2 : |x_1|, |x_2| < 1/2\}$ ,  $m \in \mathbb{Z}$ . This leads to

$$u(x; c) = (-i) \frac{2 \sin \frac{cx_2}{2}}{cx_2} \left( \frac{\sin \frac{cx_1 + m\pi}{2}}{cx_1 + m\pi} - \frac{\sin \frac{cx_1 - m\pi}{2}}{cx_1 - m\pi} \right).$$

- Constant in three rectangles:  $\cup_{j=1}^3 \Omega_j$  where each  $\Omega_j$  is a rectangle. We give the formula for generating the data for a fixed rectangle, then for three different rectangles, it is sufficient to apply the superposition. For a rectangular region  $\Omega = \{(x, y) \in \mathbb{R}^2 | a_1 < x_1 < a_2, b_1 < x_2 < b_2\}$  that supports constant  $q = 1$ , we can compute

$$u(x; c) = 4 \frac{\sin(\frac{a_2 - a_1}{2} cx_1) \sin(\frac{b_2 - b_1}{2} cx_2)}{c^2 x_1 x_2} e^{i(\frac{a_2 + a_1}{2} cx_1 + \frac{b_1 + b_2}{2} cx_2)}.$$

In the following, we test our algorithm step by step: first with the exact post-processed data and then with the far-field data.

**5.1.2. Noiseless and noisy post-processed data.** In this section, we first work with the exact post-processed data. This is to implement the Algorithm 4.3 by skipping the data processing Algorithm 4.1. To be more precise, we consider the following discrete data  $\{\tilde{u}(t_j, \theta_i) | 0 \leq j \leq T-1, 0 \leq i \leq M-1\}$  in the unit disk, i.e.,

$$U = \begin{pmatrix} \tilde{u}(t_0, \theta_0; c) & \tilde{u}(t_0, \theta_1; c) & \cdots & \tilde{u}(t_0, \theta_{M-1}; c) \\ \tilde{u}(t_1, \theta_0; c) & \tilde{u}(t_1, \theta_1; c) & \cdots & \tilde{u}(t_1, \theta_{M-1}; c) \\ \vdots & \vdots & \ddots & \vdots \\ \tilde{u}(t_{T-1}, \theta_0; c) & \tilde{u}(t_{T-1}, \theta_1; c) & \cdots & \tilde{u}(t_{T-1}, \theta_{M-1}; c) \end{pmatrix}.$$

where  $\{t_j, \omega_{t_j}\}_{j=0}^{T-1}$  are the Gauss-Legendre quadrature nodes and weights,  $\{\theta_i = \frac{2i\pi}{M}, \omega_{\theta_i} = \frac{2\pi}{M}\}_{i=0}^{M-1}$  are the trapezoidal quadrature nodes and weights, and

$$\tilde{u}(t_j, \theta_i; c) = u(p_n; c), \quad \{p_n\}_{n=1}^{TM} = \left\{ \sqrt{(t_j + 1)/2} (\cos \theta_i, \sin \theta_i)^T \right\}_{j=0, i=0}^{T-1, M-1}.$$

Here  $u(x; c)$  is given by evaluating (5.1) analytically. In Algorithm 3.1 we set  $K = 146$  in (3.9) which is sufficient for all of our experiments.

We add random uniformly distributed noise of noise level  $\delta$  to each entry of  $U$  to get the noisy matrix  $U^\delta$ , i.e.,

$$(5.2) \quad \tilde{u}^\delta(t_j, \theta_i) = \tilde{u}(t_j, \theta_i) (1 + \delta \xi_{ji}), \quad 0 \leq j \leq T - 1, 0 \leq i \leq M - 1$$

where  $\xi_{ji}$  is a uniformly distributed random number between  $-1$  and  $1$ .

It is observed that the prolate eigenvalues  $\alpha_{m,n}$  decay to zero exponentially fast and the dominant prolate eigenvalues have the same numerical magnitude. See Figure 2 for an illustration. We choose to implement Algorithm 4.3 by choosing a spectral cutoff  $\epsilon$  by

$$\epsilon = \begin{cases} 0.1|\alpha_{0,0}(c)|, & \delta = 0, & \text{(Case: Born data or analytic data)} \\ \delta|\alpha_{0,0}(c)|, & \delta \neq 0, & \text{(Case: Born data or analytic data)} \\ 0.9|\alpha_{0,0}(c)|, & & \text{(Case: simulation data)} \end{cases}$$

where  $\delta$  is the noise level.

First we test the algorithm for  $q$  being one of the disk PSWFs and we gradually perform more complicated examples. In Figure 3 we plot the ground-truth of  $q$  (left) and reconstruction of  $q$  (right). The reconstruction is under our expectation. We

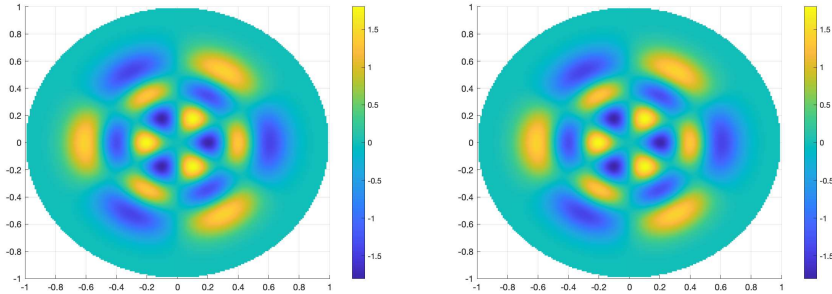


Fig. 3: Reconstruction of a disk PSWF. Left:  $\psi_{3,2,2}(x; 30)$ , right: reconstruction.

further test the performance of our algorithm for the three different types of unknowns: constant  $q$  in a disk, constant  $q$  in a rectangle, and oscillatory function  $q$ . Here the disk is given by

$$\{(x_1, x_2) \in \mathbb{R}^2 : \sqrt{x_1^2 + x_2^2} < 1/2\},$$

the rectangle is given by

$$\{(x_1, x_2) \in \mathbb{R}^2 : -1/2 < x_1, x_2 < 1/2\},$$

and the oscillatory function is given by

$$\sin(8\pi x_1) \text{ supported in } \{(x_1, x_2) \in \mathbb{R}^2 : -1/2 < x_1, x_2 < 1/2\}.$$

Numerical experiments in Figure 4 demonstrate the capability of our algorithm.

Next, we consider perturbed noisy data given by (5.2) where we add  $\delta = 20\%$  to the exact data  $U$ . The reconstruction is plotted in the bottom row of Figure 4 which shows that the algorithm is robust to the added uniform noises. We report that we also tried Gaussian noises and observed similar performance.

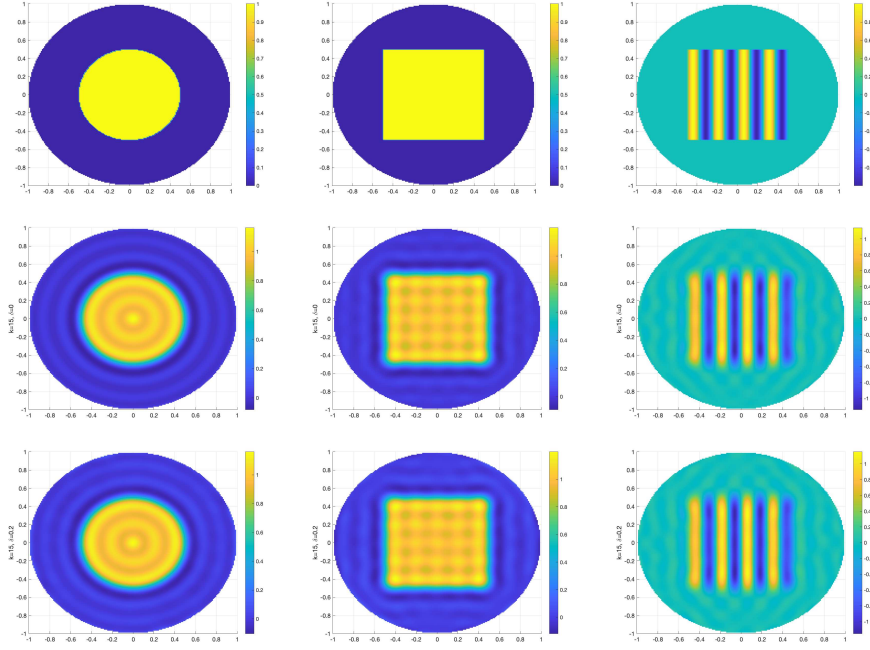


Fig. 4: Reconstruction of three different types of unknowns. First row: exact. Second row: Noiseless data. Third row: 20% noisy data.

**5.1.3. Resolution.** We emphasize the case of three rectangles to demonstrate that our algorithm's capability in improved resolution. The three rectangles are given by

$$\begin{aligned}\Omega_1 &= \{(x_1, x_2) \in \mathbb{R}^2 : -0.3 < x_1 < -0.025, 0.1 < x_2 < 0.3\}, \\ \Omega_2 &= \{(x_1, x_2) \in \mathbb{R}^2 : 0.025 < x_1 < 0.3, 0.1 < x_2 < 0.3\}, \\ \Omega_3 &= \{(x_1, x_2) \in \mathbb{R}^2 : -0.1 < x_1 < 0.1, -0.2 < x_2 < 0.025\},\end{aligned}$$

which gives the smallest distance between the rectangles 0.05. The reconstruction in Figure 5 is for noisy data with 20% noise level and  $c = 2k = 30$ . The distance is less than half wavelength  $\frac{\pi}{k} \approx 0.2$  and these objects can be clearly distinguished from the reconstruction. We point out that a similar improved resolution was also reported in [24].

**5.1.4. Far-field data.** Having successfully tested the algorithm using the post-processed data, in this section we implement the full algorithm of Algorithm 4.3 with the Born far-field data  $\{u_b^\infty(\hat{x}_m; \theta_\ell; k) : m = 1, 2, \dots, N_1, \ell = 1, 2, \dots, N_2\}$ . We follow the same rule as in (5.2) to add perturbed noise instead to the data  $\{u_b^\infty(\hat{x}_m; \hat{\theta}_\ell; k) : m = 1, 2, \dots, N_1, \ell = 1, 2, \dots, N_2\}$ .

To illustrate the potential of our algorithm in dimensionality reduction, we work with far-field data of dimension  $N_1 \times N_2 = 50 \times 50, 100 \times 100, 200 \times 200, 500 \times 500$ . The test is done with  $c = 30$ . Results in Figure 6 show that our algorithm has the potential to reduce the dimensionality of large-scale data.

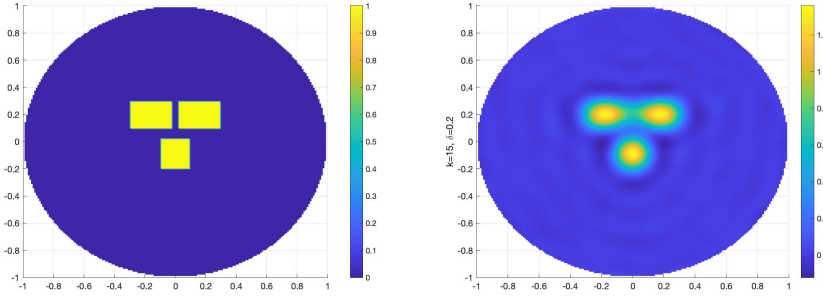


Fig. 5: Reconstruction of three close rectangles. Left: exact contrast, right: reconstruction. 20% noisy data.

**5.1.5. Increasing stability.** Another interesting aspect is the increasing stability (cf. [22, 43]): the resolution becomes better as  $c = 2k$  gets larger. We first demonstrate this property by the Born far-field data. Figure 7 plots the reconstruction of three rectangles using our method for  $k = 15, 20, 25, 30, 35, 40$ . Clearly, we have observed the increasing stability. For  $k = 40$ , the reconstruction is almost the same as the ground-truth.

Furthermore, we will test this property using the far-field data obtained by the nonlinear model in Section 5.2.2.

**5.1.6. Comparison with Matlab built-in fft.** In this section, we compare our algorithm with the Matlab built-in function `fft`. The reason is that the Born data is related to the restricted Fourier transform of the unknown  $q$ , therefore it makes sense to consider solving the unknown  $q$  by the fast Fourier transform. To apply the Matlab built-in function `fft`, the number of rectangular sampling points  $m$  is connected with wave number  $k$ , i.e.,  $m = \frac{4k}{\pi}$ , where  $k$  needs to be a multiple of  $\pi$ . We point the readers to the fractional Fourier transform [25] which overcame this issue but we only consider the Matlab built-in `fft`.

For both methods, we use noisy Born far-field data  $\{u_b^{\infty, \delta}(\hat{x}_i; \hat{\theta}_j; k)\}_{i=1, j=1}^{N_1, N_2}$  with  $N_1 = N_2 = 100$ , and noise level  $\delta = 20\%$ . For the method based on the low-rank structure, we directly apply Algorithm 4.3. For the Matlab `fft` algorithm, exact nodes are given by  $\{(i - \frac{m}{2})\frac{2}{m}, (j - \frac{m}{2})\frac{2}{m}\}_{i=0, j=0}^{m-1}$  where  $m = \frac{4k}{\pi}$  is an even number; following the idea of Algorithm 4.1, we also find the approximate or mock-quadrature nodes that are approximations to the `fft` exact nodes. For low wavenumber  $k$ , the reconstruction of our algorithm is better than that of the `fft` method; for high wavenumber  $k$ , these two methods perform similarly, see Figure 8.

**5.2. Full model.** In practical application, full far-field data  $u^\infty(\hat{x}; \hat{\theta}; k)$  are measured rather than Born far-field data  $u_b^\infty(\hat{x}; \hat{\theta}; k)$ . This motivates us to test our algorithm with the full far-field data  $\{u^\infty(\hat{x}_i; \hat{\theta}_j; k)\}$  to understand the limitations and potentials.

**5.2.1. Data generation.** For the full model, we use IPscatt [8] to generate the exact far-field data  $\{u^\infty(\hat{x}_i; \hat{\theta}_j; k)\}_{i=1, j=1}^N$ , where  $N$  denotes the number of incident directions and observation directions. The noisy data  $\{u^{\infty, \delta}(\hat{x}_i; \hat{\theta}_j; k)\}_{i=1, j=1}^N$  are generated by adding noise with noise level  $\delta$  to the simulated data  $\{u^\infty(\hat{x}_i; \hat{\theta}_j; k)\}_{i=1, j=1}^N$ .

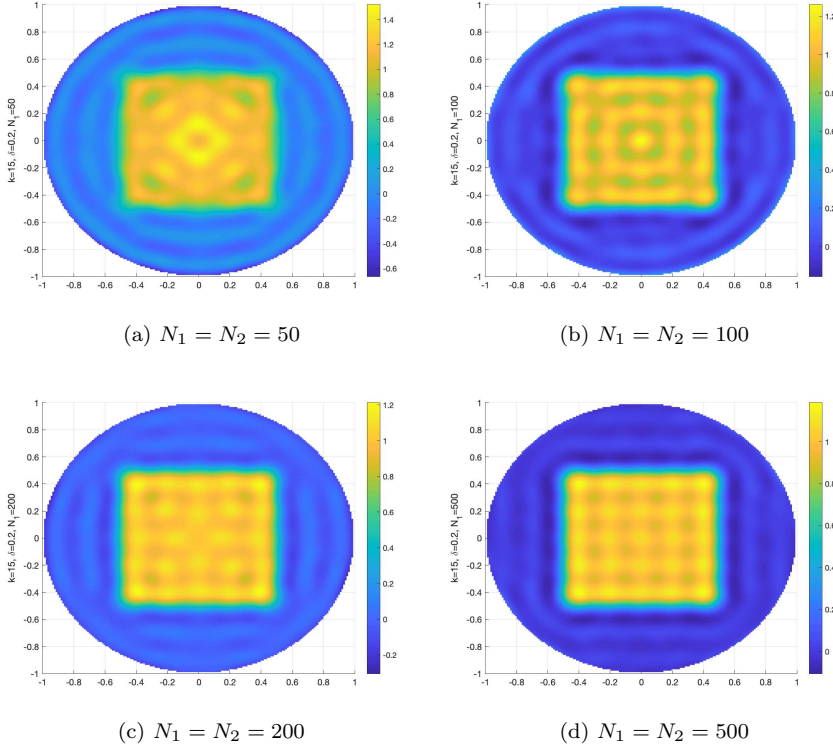


Fig. 6: Reconstruction of a rectangle with 20% noisy far-field data of dimension  $N_1 \times N_2 = 50 \times 50, 100 \times 100, 200 \times 200, 500 \times 500$ .

following (5.2). According to [8], the relative error between the Born model and the full model is given by  $\text{rel}(k) = \frac{\|U_b^s - U^s\|_2}{\|U^s\|_2}$ , where  $U_b^s = (u_{b,j}^s(x_i))_{\text{IncNb} \times \text{Np}}$ ,  $U^s = (u_j^s(x_i))_{\text{IncNb} \times \text{Np}}$  are two matrices: here  $\text{Np}$  is the number of nodes in a fixed domain  $\tilde{\Omega} = (-\sqrt{2}/2, \sqrt{2}/2) \times (-\sqrt{2}/2, \sqrt{2}/2)$  (here we follow [8] to choose  $\tilde{\Omega}$ ) and  $\text{IncNb}$  is the number of incident directions; the subindex  $j$  represents that the scattered wave is due to an incident wave at direction  $\hat{\theta}_j$ .

Note that the simulation of the far-field data of [8] makes no use of disk PSWFs, therefore the possibility of inverse crimes is avoided. In the following experiments, the spectral cutoff is set as  $\epsilon = 0.9|\alpha_{0,0}(c)|$  to incorporate that no a priori information on the relative modeling error is known.

**5.2.2. Increasing stability.** In this section, we test our algorithm by adding 20% uniform noises to the full far-field data simulated by IPscatt [8]. The number of incident and observation directions are fixed as  $N_1 = N_2 = 100$ . The modeling error is given by  $\text{rel}(k)$  for different wavenumber  $k$ .

We begin with an experiment with  $q$  supported in three rectangles. Figure 9 displays the reconstructions of the three rectangles at wavenumbers  $k \in \{15, 30, 45\}$ . Increasing the value of wave number  $k$  leads to better reconstruction under the premise that the relative modeling error is not too large.

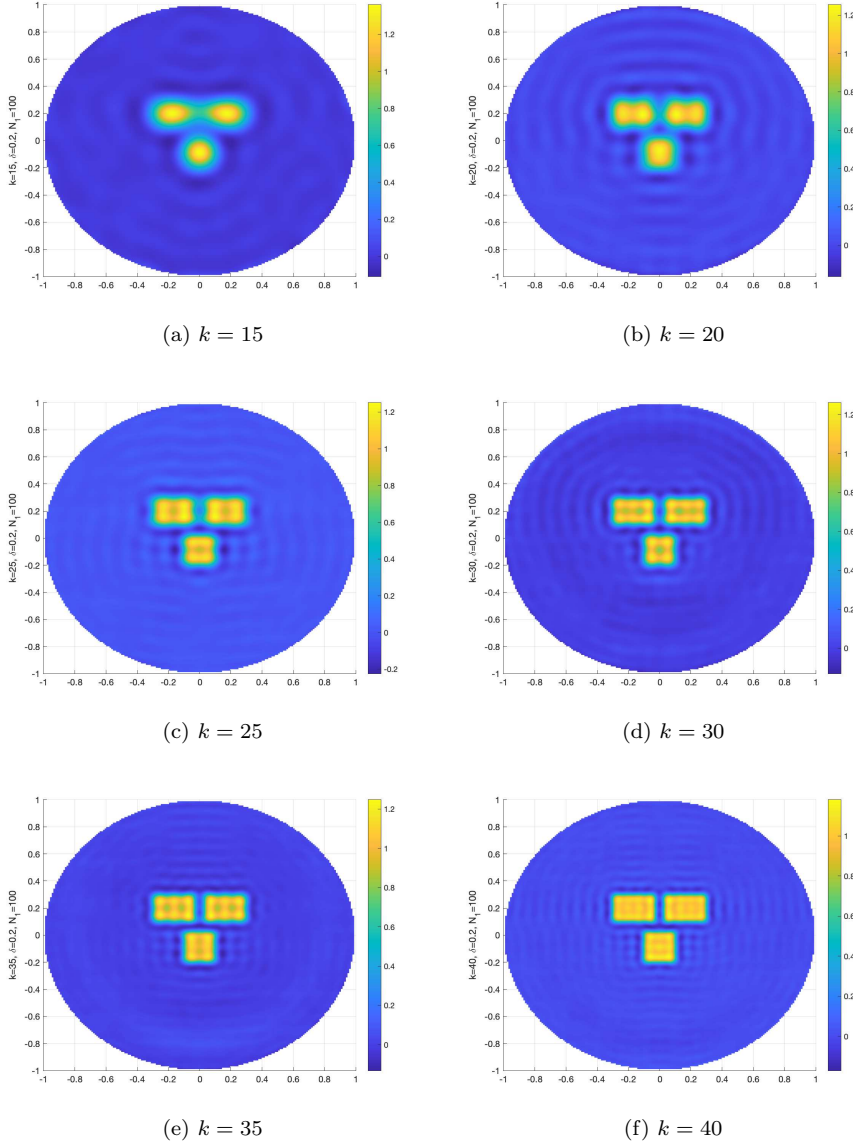


Fig. 7: Reconstruction of three rectangles using our method for  $k = 15, 20, 25, 30, 35, 40$  using 20% noisy data.

Next we consider a more complicated example where the ground-truth of the unknown  $q$  is given by Figure 10 and can be generated by Matlab function “ship2D.m” in IPscatt [8]. The distance between two small squares is  $1/16$ . Again we have observed the resolution becomes better as the wavenumber  $k$  gets larger.

We continue to test the algorithm when the relative modeling error is not small by choosing  $k \in \{60, 75\}$ . In this case, we have to use a larger data set,  $N_1 \times N_2 = 200 \times 200$ . The reconstruction remains good when the relative modeling error is

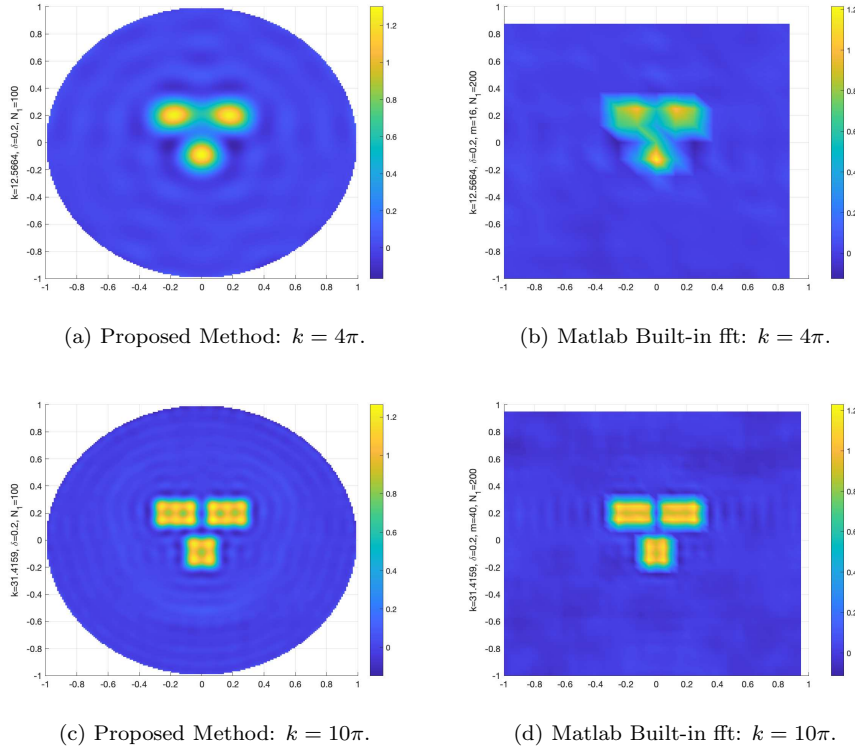


Fig. 8: Reconstruction of three rectangles. Noise level 20%.

around 35%.

**5.2.3. Comparison with an iterative reconstruction method.** In this section we compare our algorithm with IPscatt’s iterative method. Iterative methods usually depend on the choice of initial guess, are computationally expensive, and may suffer from local minima. In Figure 12, the initial guess of IPscatt’s iterative method is zero, and we run the iterative method with the number of iterations  $\text{pdaN} = 100$ . We also report that the result with number of iterations  $\text{pdaN} = 50$  is similar. Our algorithm does not require any initial guess and the numerical experiments show that it gives very good reconstructions for relative modeling error less than 50%. Our algorithm is a direct method which is more efficient than the iterative method. However, we note that our algorithm does not work for very large modeling error, say larger than 100%. One future direction is to utilize our algorithm with other nonlinear techniques to deal with nonlinear model with very large modeling errors.

**5.2.4. Far-field data extrapolation.** When the data set  $\{u^\infty(\hat{x}_i; \hat{\theta}_j; k)\}_{i=1, j=1}^{N_1, N_2}$  is of small scale, one idea is to perform Fourier interpolation to have an extrapolated data set of dimension  $\tilde{N}_1 \times \tilde{N}_2$  such that  $\tilde{N}_1, \tilde{N}_2$  are larger and then apply our proposed algorithm. In Figure 13, we use fft interpolation to extrapolate the far-field data and then apply our proposed algorithm. The first row is to reconstruct contrast  $q(x) = 0.02$  supported in a rectangle  $\Omega = \{x \in \mathbb{R}^2 : |x_1|, |x_2| < 1/2\}$  with  $N_2 = N_1 = 16$  and  $\tilde{N}_2 = \tilde{N}_1 = 128$ , and the second row is to reconstruct contrast “ship2D” with

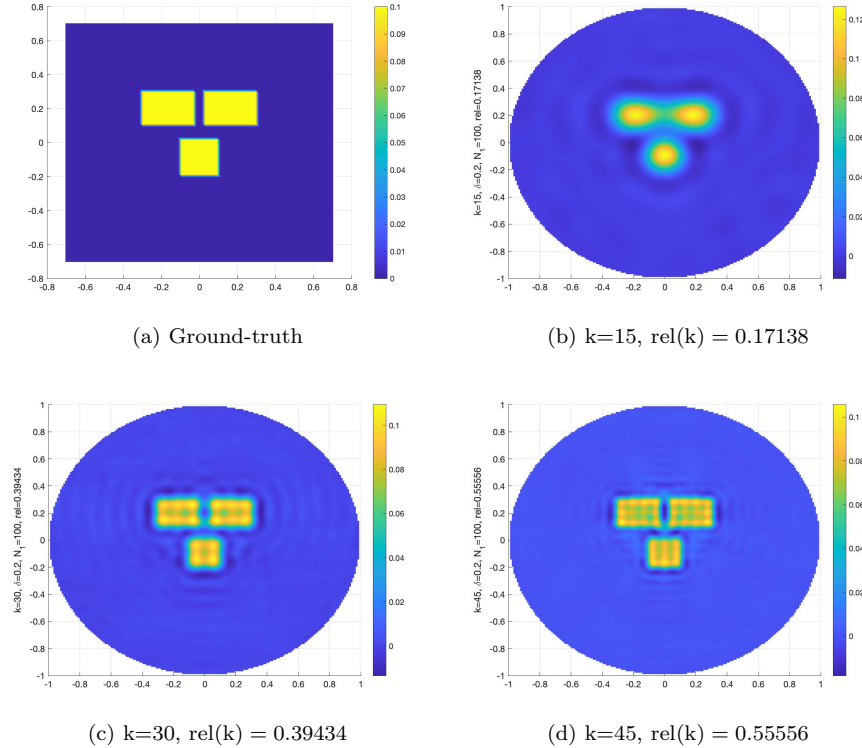
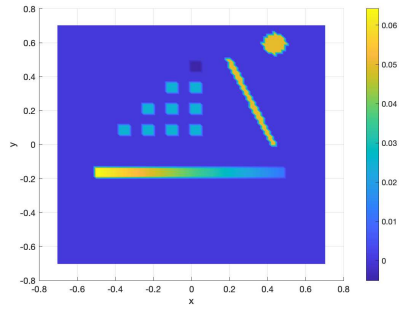


Fig. 9: Reconstruction of three rectangles using our proposed method and 20% noisy full far-field data for  $k = 15, 30, 45$ .

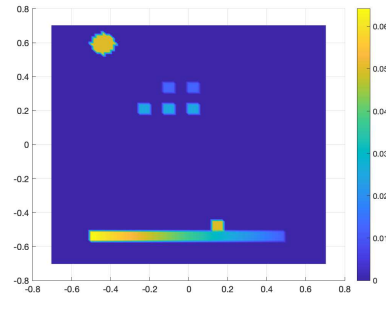
$N_2 = N_1 = 35$  and  $\tilde{N}_2 = \tilde{N}_1 = 140$ . We observe that the unknowns can still be reasonably identified.

REFERENCES

- [1] M Abramowitz and A Irene, eds. *Handbook of Mathematical Functions With Formulas, Graphs, and Mathematical Tables*, Washington: U.S. Govt. Print. Off., 1964.
- [2] L Audibert and H Haddar. A generalized formulation of the linear sampling method with exact characterization of targets in terms of far-field measurements, *Inverse Problems* **30**, 035011, 2015.
- [3] L Audibert and S Meng. Shape and parameter identification by the linear sampling method for a restricted Fourier integral operator, *Inverse Problems* **40** (9), 095007, 2024.
- [4] M Bachmayr. Low-rank tensor methods for partial differential equations, *Acta Numerica*, pp 1–121, 2023.
- [5] J Boyd. Algorithm 840: computation of grid points, quadrature weights and derivatives for spectral element methods using prolate spheroidal wave functions—prolate elements, *ACM Trans. Math. Software* **31**, no. 1, 149–165, 2005.
- [6] J Boyd and F Xu. Divergence (Runge Phenomenon) for least-squares polynomial approximation on an equispaced grid and Mock–Chebyshev subset interpolation, *Applied Mathematics and Computation* **210**, pp. 158–168, 2009.
- [7] A Bukhgeim. Recovering a potential from Cauchy data in the two dimensiona case, *Jour. Inverse Ill-Posed Problems* **16**, pp. 19–33. 2008.
- [8] F Bürgel, K Kazimierski, and A Lechleiter. Algorithm 1001: Ipscatt-a matlab toolbox for the



(a) Ground-truth, real part



(b) Ground-truth, imaginary part

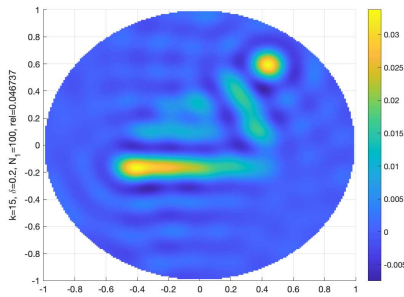
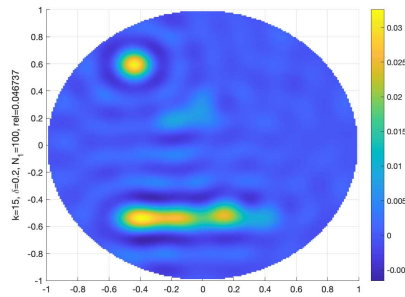
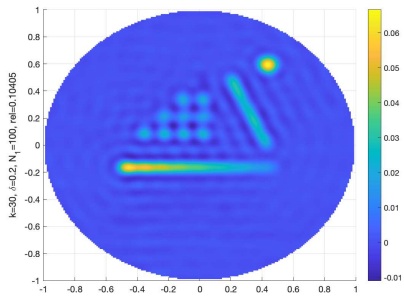
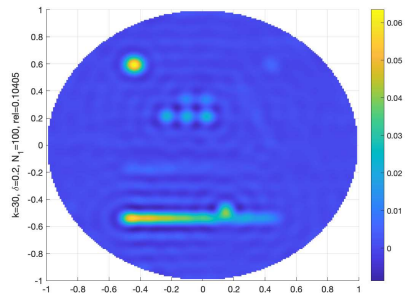
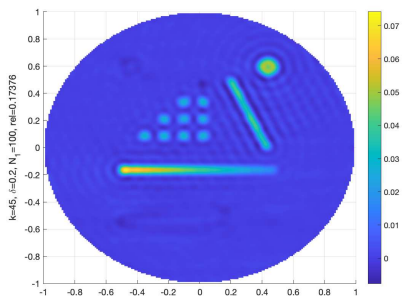
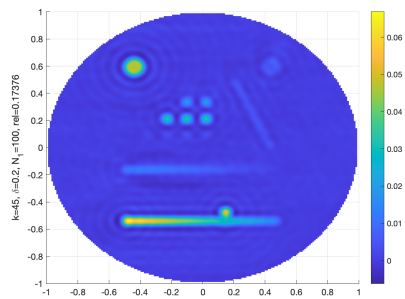
(c)  $k=15$ ,  $\text{rel}(k) = 0.046737$ , real part(d)  $k=15$ , imaginary part(e)  $k=30$ ,  $\text{rel}(k) = 0.10405$ , real part(f)  $k=30$ , imaginary part(g)  $k=45$ ,  $\text{rel}(k) = 0.17376$ , real part(h)  $k=45$ , imaginary part

Fig. 10: Reconstruction of “ship2D” contrast using 20% noisy full far-field data for  $k = 15, 30, 45$ . Left column: real part, right column: imaginary part.

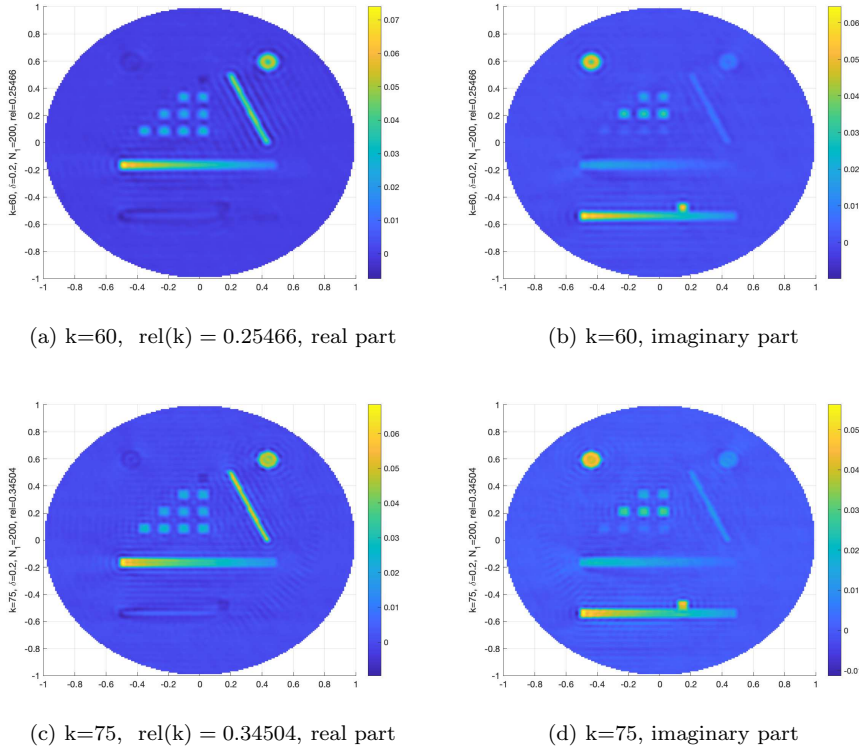


Fig. 11: Reconstruction using 20% noisy full far-field data for  $k \in \{60, 75\}$ .

inverse medium problem in scattering, *ACM Trans. Math. Software* **45**(4), 2019.

[9] F Cakoni and D Colton. *Qualitative Approach to Inverse Scattering Theory*, Springer, 2016.

[10] F Cakoni, D Colton and H Haddar. *Inverse Scattering Theory and Transmission Eigenvalues*, CBMS-NSF, SIAM Publications **98**, 2nd Edition, 2023.

[11] D Colton and A Kirsch. A simple method for solving inverse scattering problems in the resonance region, *Inverse Problems* **12**, pp. 383–393, 1996.

[12] D Colton and R Kress. *Inverse Acoustic and Electromagnetic Scattering Theory*, Springer Nature, New York, 2019.

[13] C Cortes and V Vapnik. Support-vector networks, *Machine learning* **20**, pp. 273–297, 1995.

[14] Y Gao, H Liu, X Wang, and K Zhang. On an artificial neural network for inverse scattering problems, *Journal of Computational Physics* **448**, 110771, 2022.

[15] I Goodfellow, Y Bengio, and A Courville. *Deep learning*, MIT press, 2016.

[16] D Gottlieb and O Steven. *Numerical analysis of spectral methods: theory and applications*, Society for Industrial and Applied Mathematics, 1977.

[17] P Greengard. Generalized prolate spheroidal functions: algorithms and analysis, *Pure and Applied Analysis* **6** (3), , pp. 789–833, 2024.

[18] P Greengard and K Serkh. On generalized prolate spheroidal functions –Preliminary Report, *Technical Report YALEU/DCS/TR-1542*, 2018.

[19] R Griesmaier and C Schmiedecke. A factorization method for multifrequency inverse source problems with sparse far-field measurements, *SIAM Journal on Imaging Sciences* **10**, pp. 2119–2139, 2017.

[20] W Hackbusch. *Tensor Spaces and Numerical Tensor Calculus*, second edition, Springer, 2019.

[21] T Hofmann, B Schölkopf, and A J. Smola. Kernel methods in machine learning, *The Annals of Statistics*, **36**, pp. 1171–1220, 2008.

[22] T Hrycak and V Isakov. Increased stability in the continuation of solutions to the helmholtz equation, *Inverse Problems* **20**(3):697–712, 2004.

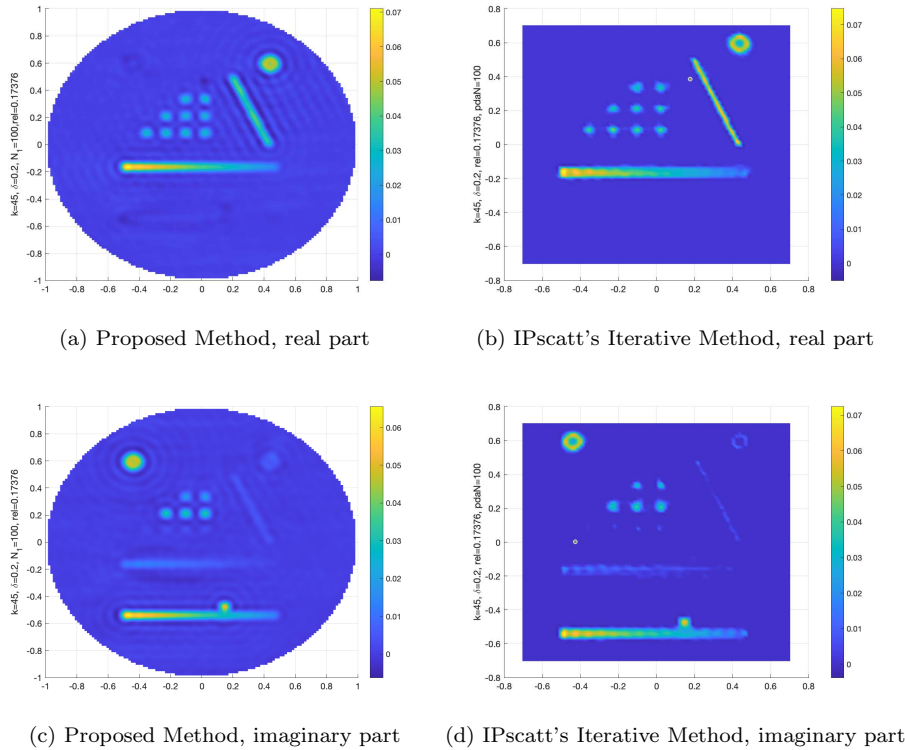


Fig. 12: Reconstruction of “ship2D” contrast using the our proposed algorithm and IPscatt’s iterative method with  $k = 45$ .

- [23] M Isaev and R Novikov. Reconstruction from the Fourier transform on the ball via prolate spheroidal wave functions, *Journal de Mathématiques Pures et Appliquées* **163**, pp.318–333, 2022.
- [24] M Isaev, R Novikov, G Sabinin. Numerical reconstruction from the Fourier transform on the ball using prolate spheroidal wave functions, *Inverse Problems* **38**, 105002, 2022.
- [25] G Inverarity. Fast computation of multidimensional fourier integrals, *SIAM Journal on Scientific Computing* **24**(2), 2002.
- [26] Y Khoo and L Ying. SwitchNet: a neural network model for forward and inverse scattering problems, *SIAM J. Sci. Comput.* **41** no. 5, A3182–A3201, 2019.
- [27] A Kirsch. Characterization of the shape of a scattering obstacle using the spectral data of the far-field operator, *Inverse Problems* **14**, pp. 1489–1512, 1998.
- [28] A Kirsch. Remarks on the Born approximation and the Factorization Method, *Applicable Analysis* **96**, no. 1, pp. 70–84, 2017.
- [29] Y Li, X Cheng, and J Lu. Butterfly-Net: optimal function representation based on convolutional neural networks, *Commun. Comput. Phys.* **28** No. 5, pp.1838–1885, 2020.
- [30] Y Liu, Z Wu, J Sun, and Z Zhang. Deterministic-statistical approach for an inverse acoustic source problem using multiple frequency limited aperture data, *Inverse Problems and Imaging* **17**(6), 1329–1345, 2024.
- [31] S Meng. Data-driven basis for reconstructing the contrast in inverse scattering: Picard criterion, regularity, regularization, and stability, *SIAM J. Appl. Math.* **83** (5), 2003–2026, 2023.
- [32] S Meng and B Zhang. A kernel machine learning for inverse source and scattering problems, *SIAM J. Numer. Anal.* **62** (3), 1443–1464, 2024.
- [33] K Li, B Zhang and H Zhang. Reconstruction of inhomogeneous media by an iteration algorithm with a learned projector, *Inverse Problems* **40**, pp. 075008, 2024.

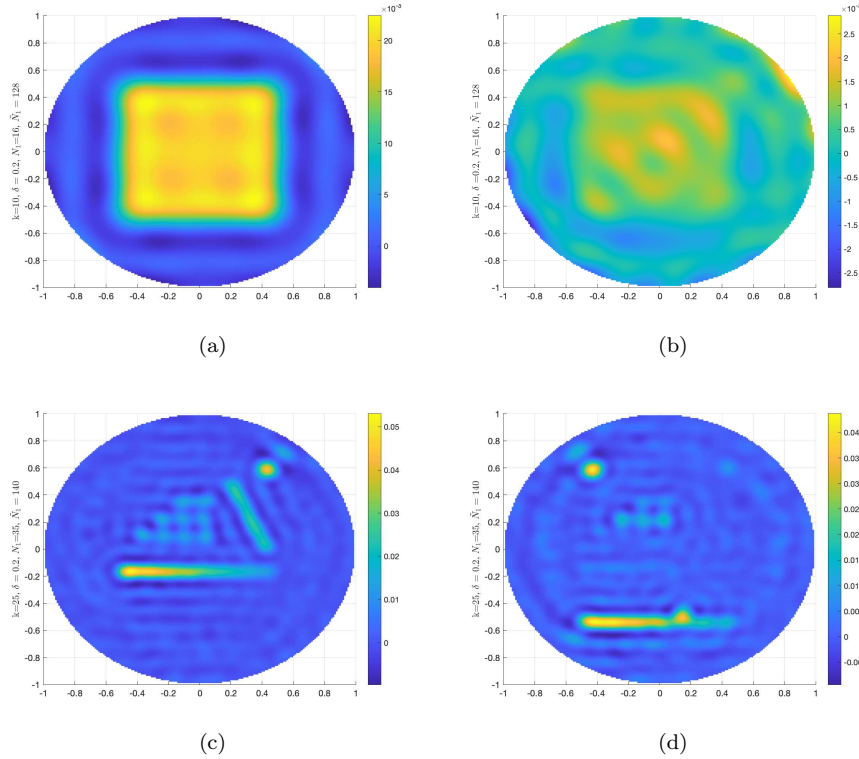


Fig. 13: Reconstruction using extrapolated data generated by Fourier interpolation. Left column: real part, right column: imaginary part.

[34] S Moskow and J Schotland. Convergence and stability of the inverse Born series for diffuse waves, *Inverse Problems* **24**, 065004, 2008.

[35] J Ning, F Han, and J Zou. A direct sampling-based deep learning approach for inverse medium scattering problems, *Inverse Problems* **40**, pp. 015005, 2023.

[36] J Osborn. Spectral approximation for compact operators, *Math. Comp.* **29**, pp.712–725, 1975.

[37] A Osipov, V Rokhlin, and H Xiao. *Prolate spheroidal wave functions of order zero*, Springer Ser. Appl. Math. Sci. 187, 2013.

[38] A Quarteroni, R Sacco and F Saleri. *Numerical Mathematics*, Springer, 2000.

[39] Y Shkolnisky. Prolate Spheroidal Wave Functions on a disc – Integration and approximation of two-dimensional bandlimited functions, *Appl. Comput. Harmon. Anal.* **22**: 235–256, 2007.

[40] D Slepian and H Pollak. Prolate Spheroidal Wave Functions, Fourier Analysis and Uncertainty -I, *Bell System Tech. J.* **40**, pp. 43–64, 1961.

[41] D Slepian. Prolate Spheroidal Wave Functions, Fourier Analysis and Uncertainty -IV: Extensions to Many Dimensions; Generalized Prolate Spheroidal Functions, *Bell System Tech. J.* **43**, pp. 3009–3057, 1964.

[42] D Slepian. Prolate spheroidal wave functions, Fourier analysis, and uncertainty V: The discrete case, *Bell System Tech. J.* **57**, pp.1371–1430, 1978.

[43] D Subbarayappa and V Isakov. On increased stability in the continuation of the helmholtz equation. *Inverse Problems* **23** no.4, pp. 1689–1697, 2007.

[44] A Weideman. Numerical integration of periodic functions: A few examples, *The American mathematical monthly* **109**, no. 1, pp. 21–36, 2002.

[45] J Zhang, H Li, L-L Wang and Z Zhang. Ball prolate spheroidal wave functions in arbitrary dimensions, *Appl. Comput. Harmon. Anal.* **48**, no. 2, pp. 539–569, 2020.